Supplementary Information for 'Active Tension Network model suggests an exotic mechanical state realized in epithelial tissues'

Nicholas Noll,[1] Madhav Mani,[2] Idse Heemskerk,[3] Sebastian J. Streichan,[1,4] and Boris I. Shraiman[1,4]

[1] *Department of Physics, University of California Santa Barbara*

[2] *Department of Applied Mathematics, Northwestern University*

[3] *Department of Biosciences, Rice University*

[4] *Kavli Institute for Theoretical Physics*

CONTENTS

I. DERIVATION OF COMPATIBILITY CONDITION AND CONSTRUCTION OF DUAL TRIANGULATION

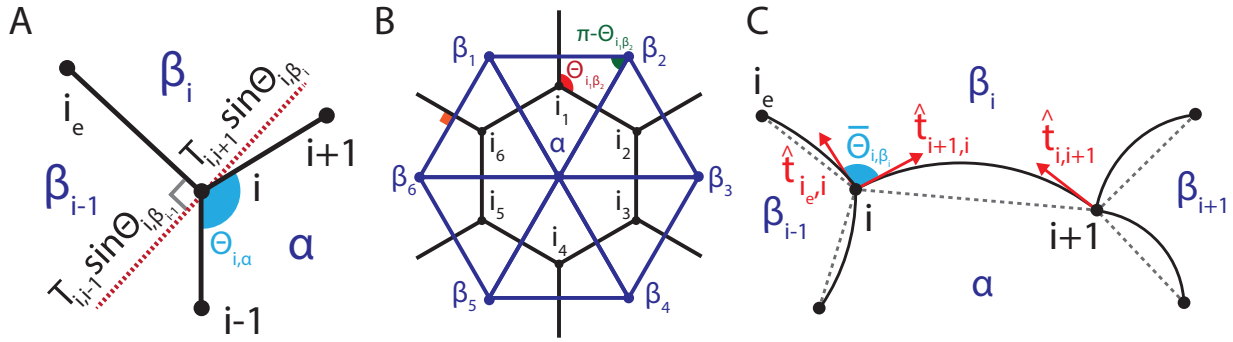

FIG. 1. (A) Mechanical balance of a tension net implies that at vertex i, $T_{i,i-1}\sin(\theta_{i,\beta_{i-1}}) = T_{i,i+1}\sin(\theta_{i,\beta_i})$, as tensions must balance along the direction perpendicular to the edge external to cell α. This construction can be repeated on all vertices of cell α. The circular product of such ratios around a cell is defined as the 'compatibility condition'. (B) A diagram representing both the notation used to define the compatibility constraint and the "dual triangulation" of the tension plane which corresponds to the tension balanced state. Edges of the $\alpha\beta_1\beta_2$ triangle represent tensions that balance at vertex i_1, while angles (of the triangle) are complementary to the angles of the corresponding vertex of the polygonal cell array (e.g. $\angle\alpha\beta_2\beta_1 = \pi - \theta_{i_1\beta_2}$. Note that compatibility condition on cell α can be alternatively derived from applying the sine theorem to the triangles that meet at dual vertex α. (C) The geometry of force balance in the generalized vertex model [1] allowing for non-uniform pressure, is modified as edges between cell with unequal pressure are circular arcs with curvatures given by the Young-Laplace law. Assuming that pressure differences are small (compared to tensions) this can be used to derive the expected non-zero value for χ_α.

The compatibility condition (c.f. Eq (5) in the main text) on cellular geometry is the natural result from our model assumptions that (i) tissues are in mechanical equilibrium and (ii) tissue mechanics is dominated by tension held in the cortical cytoskeleton. The purpose of this section is to provide a derivation of Eq. (5) as well as our 'dual' tension triangulation. Consider vertex 'i', depicted in Fig. 1a, formed by the triplet of cells $(\alpha, \beta_{i-1}, \beta_i)$. Force balance at this vertex is written $T_{i,i_e}\hat{\boldsymbol{r}}_{i_e,i} + T_{i,i+1}\hat{\boldsymbol{r}}_{i+1,i} + T_{i,i-1}\hat{\boldsymbol{r}}_{i-1,i} = 0$. Projecting this equation onto the red-line as shown in Fig 1a

$$T_{i,i+1}\left[\hat{\boldsymbol{r}}_{i_e i}\wedge\hat{\boldsymbol{r}}_{i_+ i}\right] = T_{i,i-1}\left[\hat{\boldsymbol{r}}_{i_- i}\wedge\hat{\boldsymbol{r}}_{i_e i}\right] \implies \frac{T_{i,i+1}}{T_{i,i-1}} = \frac{\sin\left(\theta_{i,\beta_{i-1}}\right)}{\sin\left(\theta_{i,\beta_i}\right)} \tag{1}$$

This construction can be done for each vertex belonging to a cellular plaquette. Indexing vertices belonging to cell α using a CCW convention with $i \in \{1, 2, ..., z_\alpha\}$, as shown in Fig. 1b, we take the circular product around the cell and define the "geometric compatibility" measure χ_α

$$\chi_\alpha = \prod_{i=1}^{z_\alpha} \frac{\sin\left(\theta_{i,\beta_i}\right)}{\sin\left(\theta_{i,\beta_{i-1}}\right)} = \prod_{i=1}^{z_\alpha} \frac{T_{i,i-1}}{T_{i,i+1}} = 1 \tag{2}$$

The circular product over the ratios of tensions is a telescoping product and thus is equal to one for a static tension net, which we call the compatibility condition. As noted in the main text, this geometric constraint can be directly tested on images to assess the validity of model assumptions. A corollary to the compatability condition is that tensions form a triangulation 'dual' to the cell array. Once again consider force-balance at vertex 'i', but this time rotated by $\pi/2$

$$\hat{\boldsymbol{z}}\wedge\left[T_{i,i_e}\hat{\boldsymbol{r}}_{i_e,i} + T_{i,i+1}\hat{\boldsymbol{r}}_{i+1,i} + T_{i,i-1}\hat{\boldsymbol{r}}_{i-1,i}\right] = \boldsymbol{q}_{\beta_{i-1}\beta_i} + \boldsymbol{q}_{\beta_i\alpha} + \boldsymbol{q}_{\alpha\beta_{i-1}} = 0 \tag{3}$$

where $\boldsymbol{q}_{\alpha\beta_{i-1}}, \boldsymbol{q}_{\beta_i\alpha}, \boldsymbol{q}_{\beta_{i-1}\beta_i}$ are vectors that make up edges of the triangle dual to vertex i, shared by cells $\alpha, \beta_i, \beta_{i-1}$. We have $\boldsymbol{q}_{\alpha\beta} = \boldsymbol{Q}_\alpha - \boldsymbol{Q}_\beta$ where $\boldsymbol{Q}_\alpha$ denotes the vertex of the dual triangulation that corresponds

to cell α. Summing around vertices belonging to a cellular plaquette will cancel out internal dual vectors and leave us with

$$\sum_i \boldsymbol{q}_{\beta_{i-1}\beta_i} = 0 \tag{4}$$

In other words, the outside edges of all triangles made from tensions acting at vertices around a cell must form a *closed polygon*, ensuring that we can build a closed triangulation out of tensions. This is equivalent to the constraint that $\sum_i \theta_{i,\alpha} = 2\pi$. One can then see that the compatibility constraint is simply the law of sines applied to triangles around the plaquette! Lastly, it is important to note that this construction only defines the triangulation up to a scale reflecting the fact that at equilibrium all tensions are known up to an overall multiplicative factor.

The compatibility constraint is a necessary condition for mechanical equilibrium under conditions of tension dominance. Its failure would imply either that (i) the tissue is not in mechanical equilibrium or that (ii) forces other than cortical tension contribute significantly to the balance. Observed fluctuations make it clear that mechanical equilibrium can only be approximate. Below we shall examine the effects of deviations from mechanical equilibrium and deviations from tension dominance on the distribution of χ_α. To that end, we analytically derive χ_α under the assumption of weak pressure differentials and small vertex fluctuations. Note, that while being necessary, the compatibility constraint is not sufficient to conclude tension balance. E.g. it is conceivable that cell array has "compatible geometry" for a reason other than tension-net equilibrium, however, we are not aware of any alternative simple physical mechanism that would explain this geometry.

We first consider the case of small pressure differences across cell-cell contacts. Consider vertex 'i' as shown in Fig. 1c. Force balance now takes the form $T_{i,i_e}\hat{\boldsymbol{t}}_{i_e,i} + T_{i,i+1}\hat{\boldsymbol{t}}_{i+1,i} + T_{i,i-1}\hat{\boldsymbol{t}}_{i-1,i} = 0$ where $\hat{\boldsymbol{t}}_{i+1,i}$ denotes the unit vector pointing tangent to the circular arc of edge $(i, i+1)$ at vertex i instead of along the vertex model direction (shown as a gray dashed line). Repeating the derivation leading to Eq. (SI2), one arrives at

$$\frac{T_{i,i+1}}{T_{i,i-1}} = \frac{\sin\left(\bar{\theta}_{i,\beta_i}\right)}{\sin\left(\bar{\theta}_{i,\beta_{i-1}}\right)} \tag{5}$$

where $\bar{\theta}$ - and this is a crucial difference -denotes the angle between tangent vectors as opposed to polygon edges. Taking a product around the cell yields:

$$\log\left(\bar{\chi}_\alpha\right) = \sum_{i=1}^{z} \log\left[\sin\left(\bar{\theta}_{i,\beta_i}\right)\right] - \log\left[\sin\left(\bar{\theta}_{i,\beta_{i-1}}\right)\right] = 0 \tag{6}$$

To relate $\bar{\chi}_\alpha$ to χ defined in Eq (SI2) we relate angles $\bar{\theta}$ and θ. In the limit of small pressure differentials ($\Delta p\, r/T \ll 1$), the tangent vector simplifies to $\hat{\boldsymbol{t}}_{i+1,i} = \hat{\boldsymbol{r}}_{i+1,i} + \frac{\Delta p_{i+1,i}}{2T_{i,i+1}}\left[\hat{\boldsymbol{z}} \wedge \boldsymbol{r}_{i+1,i}\right]$, where $\Delta p_{i+1,i} = p_\alpha - p_{\beta_i}$ is the signed pressure difference across edge $i, i+1$). Substituting this result in and Taylor expanding to linear order we find

$$\sin\left(\bar{\theta}_{i,\beta_i}\right) \approx \sin\left(\theta_{i,\beta_i}\right)\left[1 + \cot\left(\theta_{i,\beta_i}\right)\left[\frac{\Delta p_{i+1,i}\, r_{i+1,i}}{2T_{i,i+1}} - \frac{\Delta p_{i_e,i}\, r_{i_e,i}}{2T_{i,i_e}}\right]\right] \tag{7}$$

The expected value for the compatibility condition is obtained by summing this expression around a cell.

$$\begin{aligned}\log(\chi_a) \approx & \frac{1}{2}\sum_i \left[\cot\left(\theta_{i,\beta_i}\right) + \cot\left(\theta_{i+1,\beta_i}\right)\right]\frac{r_{i+1,i}}{T_{i+1,i}}\left[p_{\beta_i} - p_\alpha\right] \\ & -\frac{1}{2}\sum_i \left[\cot\left(\theta_{i,\beta_i}\right) + \cot\left(\theta_{i,\beta_{i-1}}\right)\right]\frac{r_{i_e,i}}{T_{i_e,i}}\left[p_{\beta_i} - p_{\beta_{i-1}}\right]\end{aligned} \tag{8}$$

Thus deviation of χ_α away from 1 is a function of local pressure differences. Interestingly, one can define a local "angle defect" in the tension plane $\delta\theta_\alpha = 2\pi - \sum_i \theta_{i,\alpha} = -\frac{1}{2}\sum_i \frac{r_{i+1,i}}{T_{i+1,i}}\left[p_{\beta_i} - p_\alpha\right]$ which quantifies the

degree of local non-planarity (Gaussian curvature) of the tension triangulation (at dual vertex α). (This angle defect is exactly the discrete Laplace-Beltrami operator acting on pressure [2]).

For completeness, one can also derive the expected value for the compatibility condition under small fluctuations in vertex position $\delta \boldsymbol{r}_i$ in the same manner as above. The result is

$$\begin{aligned}\log(\chi_a) \approx & \frac{1}{2}\sum_i \left[\cot\left(\theta_{i,\beta_i}\right) + \cot\left(\theta_{i+1,\beta_i}\right)\right] \frac{\delta \boldsymbol{r}_{i,i+1} \wedge \hat{\boldsymbol{r}}_{i+1,i}}{r_{i+1,i} + \delta \boldsymbol{r}_{i,i+1} \cdot \hat{\boldsymbol{r}}_{i+1,i}} \\ & -\frac{1}{2}\sum_i \left[\cot\left(\theta_{i,\beta_i}\right) + \cot\left(\theta_{i,\beta_{i-1}}\right)\right] \frac{\delta \boldsymbol{r}_{i,i_e} \wedge \hat{\boldsymbol{r}}_{i_e,i}}{r_{i_e,i} + \delta \boldsymbol{r}_{i,i_e} \cdot \hat{\boldsymbol{r}}_{i_e,i}} \end{aligned} \tag{9}$$

II. ISOGONAL MODES AND CONFORMAL SYMMETRY.

Isogonal modes can be thought of as the discretized degrees of freedom associated to the conformal symmetry of the continuum description. The elastic energy associated to displacement field $u_a(\boldsymbol{r})$ (at position $\boldsymbol{r}$) with vanishing bulk modulus is

$$E = \frac{1}{2}\int d^2\boldsymbol{r}\left[\partial_a u_b(\boldsymbol{r}) + \partial_b u_a(\boldsymbol{r}) - \frac{1}{2}\delta_{ab}\partial_c u_c(\boldsymbol{r})\right]^2 \tag{10}$$

where $\{a, b, c\}$ label *spatial* indices. Assuming relaxational dynamics - i.e. $\dot{u}_a = -\frac{\delta E}{\delta u_a}$ - the equation of motion for field u_a is found to be $\dot{u}_a = \partial^2 u_a$. Any solution of the Cauchy-Riemann equations ($\partial_x w_x = \partial_y w_y$; $\partial_x w_y = -\partial_y w_x$) can be added to u_a with no generation of additional internal stresses. That is to say, any conformal transformation of our equilibrium displacement field is also a valid ground state. Isogonal modes correspond to such independent local dilations.

Alternatively isogonal modes can be thought of as generalizations of the Villain's iso-perimetric *breather modes* [3] of a hexagonal lattice of domain walls. Villain's model [3] in particular described adsorbed atoms on a 2D substrate, where, in the incommensurable phase, 'grain' boundaries form between 'out' of register phases. The boundary energy for regular hexagonal lattice of such domains $\sum_{ij} T\, r_{ij}$ is unchanged under breather modes generated by dilations of hexagons, which can be demonstrated to leave the total length of the entire boundary $\sum_{ij} r_{ij}$ invariant. Our isogonal modes are a generalization to the case of a general lattice (satisfying ATN equilibrium constraints) when interfacial energy varies from edge to edge $T \to T_{ij}$.

III. MODE ANALYSIS OF THE ATN MODEL FOR A 1D CABLE

Starting from Eqs (2-4) in the main text and specializing to a one-dimensional *uniform* cable of active-elements, the linearized equations become

$$\begin{aligned}\frac{d}{dt}\delta r_n &= \nu^{-1} K\bar{\ell}\left[\delta u_n - \delta u_{n-1}\right] \\ \frac{d}{dt}\delta u_n &= \nu^{-1} K\left[\delta u_{n+1} + \delta u_{n-1} - 2u_n\right] - \frac{l_0 W'[1]}{\tau_\ell u_0}(\delta u_n - \delta m_n) \\ \frac{d}{dt}\delta m_n &= \alpha\tau_\ell^{-1} W'[1]\left(\delta u_n - \delta m_n\right)\end{aligned} \tag{11}$$

We've defined 1D strain $u_n \equiv (r_{n,n+1} - \ell_n)/\bar{\ell} = T_n/K\bar{\ell}$ where $r_{n,n+1} = r_{n+1} - r_n$ the length of the edge between vertices r_{n+1} and r_n and $\bar{\ell}$ is the mean intrinsic length. We have rescaled $m \to \frac{aT_s}{K\bar{\ell}} m$ to make it dimensionless. In the continuum limit, these transform to

$$\partial_t \begin{pmatrix}\delta r \\ \delta u \\ \delta m\end{pmatrix} = \begin{pmatrix}0 & \nu^{-1}K\bar{\ell}^2\partial_x & 0 \\ 0 & \nu^{-1}K\bar{\ell}^2\partial_x^2 - \kappa & \kappa \\ 0 & \bar{\alpha} & -\bar{\alpha}\end{pmatrix}\begin{pmatrix}\delta r \\ \delta u \\ \delta m\end{pmatrix} \tag{12}$$

x denotes the coordinate along the cable. Furthermore we've defined $\kappa \equiv \frac{\bar{\ell} W'[1]}{\tau_\ell u_0}$ and $\bar{\alpha} = \alpha \tau_\ell^{-1} W'[1]$. As was expected, all elements of the first column of the matrix are zero, implying that δr displacements along the cable are zero modes and that their associated dynamics is slaved to the dynamics of tension and myosin perturbations. Hence, we focus on the reduced myosin/tension system in Fourier space (define $D \equiv \nu^{-1} K \bar{\ell}^2$)

$$\partial_t \begin{pmatrix} \tilde{u} \\ \tilde{m} \end{pmatrix} = \begin{pmatrix} -Dk^2 - \kappa & \kappa \\ \bar{\alpha} & -\bar{\alpha} \end{pmatrix} \begin{pmatrix} \tilde{u} \\ \tilde{m} \end{pmatrix} \tag{13}$$

The exact dispersion relation for both branches is

$$\lambda_{1,2} = -\frac{Dk^2 + \bar{\alpha} + \kappa}{2} \left[1 \pm \sqrt{1 - \frac{4\bar{\alpha} D k^2}{(Dk^2 + \bar{\alpha} + \kappa)^2}} \right] \tag{14}$$

Assuming mechanical feedback occurs on a slower time-scale than actomyosin contractility ($\frac{\bar{\alpha}}{\kappa} << 1$) we can expand each dispersion relation to linear order in $\frac{\bar{\alpha}}{\kappa}$

$$\lambda_{1,2} \approx -\left[Dk^2 + \kappa + \frac{\bar{\alpha}\kappa}{Dk^2 + \kappa} \right], -\frac{\bar{\alpha} D k^2}{Dk^2 + \kappa} \tag{15}$$

We immediately see that first branch is gapped by κ while the second branch is acoustic, corresponding to fact that a global rescaling of tension and myosin along the cable does not perturb the underlying force balance or stall condition and thus there are phonons at long times and length scales effectively behaving as a solid! The eigenvectors are

$$\phi_{1,2} \approx \begin{pmatrix} Dk^2 + \kappa \\ -\bar{\alpha} \end{pmatrix}, \begin{pmatrix} \kappa \\ Dk^2 + \kappa \end{pmatrix} \tag{16}$$

For $\bar{\alpha} = 0$ the gapped mode corresponds solely to tension perturbations that exponentially localize within a length scale $\sqrt{D/\kappa}$ - at short times isogonal/fluid deformations will occur within this 'droplet'. This recapitulates a passive Maxwellian viscoelasticity. Conversely, for $0 < \bar{\alpha} << \kappa$, the gapped mode is an admixture between both tension and myosin perturbations along the cable. Taken together, Eqns. (SI15) and (SI16) provide the details to the argument made in the main text. At long wavelengths, and thus small k, only the acoustic branch is non-zero. The spring constant of this mode is the second derivative of the dispersion relation at $k = 0$ and thus $K_{eff} = \bar{\alpha}\kappa^{-1} D$ as reported.

To gain further insight into the rheology of this material, we now study Eq. (SI13) under sinusoidal forcing on the boundary. We expand tension along the cable in a Fourier sine series

$$u = u_0 + u_\Delta \left(\frac{x}{L} \right) + \sum_{q=1}^{\infty} \tilde{u}_q \sin \left(\frac{q\pi x}{L} \right) \tag{17}$$

We are only interested in symmetric longitudinal pulling and thus set $u_\Delta = 0$. A similar decomposition exists for myosin line density m

$$i\omega\, \bar{u}_q + \left(D \frac{q^2 \pi^2}{L^2} + \kappa \right) \bar{u}_q - \kappa \bar{m}_q = \frac{(1 - (-1)^q)}{\pi q} \bar{F}_{ext}(\omega) = \bar{F}_q \tag{18}$$

$$i\omega \bar{m}_q + \bar{\alpha}\bar{m}_q - \bar{\alpha}\bar{u}_q = \frac{(1 - (-1)^q)}{\pi q} \bar{M}_{ext}(\omega) = \bar{G}_q \tag{19}$$

F_{ext} and M_{ext} represent the time-dependent external force acting on the boundary of the 1D chain. The dynamic boundary conditions act as a source as expected (only onto the odd modes as they respect the left/right symmetry). Eq. (SI19) implies $\bar{m}_q = \frac{\bar{G}_q + \alpha \bar{u}_q}{\alpha + i\omega}$. Substituting this into the Eq. (SI18).

$$\bar{u}_q \left[D \frac{q^2 \pi^2}{L^2} + \kappa \left(1 - \frac{\bar{\alpha}}{\bar{\alpha} + i\omega} \right) + i\omega \right] = i\omega \left[\bar{F}_q + \frac{\kappa}{\bar{\alpha} + i\omega} \bar{G}_q \right] \tag{20}$$

which can be simplified to obtain (we assume the forcing function on myosin is equivalent to the forcing function on tension)

$$\bar{u}_q(\omega) = -\frac{b^2(\omega)}{(\pi q)^2 + b^2(\omega)} \frac{(1-(-1)^q)}{\pi q} \bar{F}_{ext}(\omega) \tag{21}$$

where we defined $b^2(\omega) = i\omega L^2 D^{-1} \left[1 + \frac{\kappa}{\bar{\alpha}+i\omega}\right]$. The Fourier series over q can be re-summed to give $\bar{u}(x,\omega)$ for $x \in [-L/2, L/2]$.

$$\bar{u}(x,\omega) = \frac{\cosh(\frac{bx}{L})}{\cosh(\frac{b}{2})} \bar{F}_{ext}(\omega) \tag{22}$$

This immediately implies the phase relationship between strain and the external force is

$$\bar{r}(\omega) = -\frac{ib^2 \cosh(\frac{bx}{L})}{\omega L^2 \cosh(\frac{b}{2})} \bar{F}_{ext}(\omega) \tag{23}$$

We note this has the expected regimes of behavior discussed in the main text. For $\omega << \bar{\alpha}$, the relationship is $\bar{r} \sim D^{-1}\left[1 + \frac{\kappa}{\bar{\alpha}}\right]\bar{F}$ and thus it behaves as a spring with stiffness $\frac{\bar{\alpha}D}{\kappa+\bar{\alpha}}$ as expected from our dispersion relation derived above. For $\bar{\alpha} << \omega << \kappa$ the relationship is $\bar{r} \sim \frac{i\kappa}{D\omega}\bar{F}$ and thus it behaves as a visco-elastic fluid, probing the gap between acoustic and optical branch. This regime is where isogonal deformations and localized stress patterns should exist. Lastly, if $\omega >> \kappa$ then $\bar{r} \sim D^{-1}\bar{F}$ - i.e. we are simply pulling on the elastic cytoskeletal network. The results provide an analytic backbone to the numerical results obtained for a $2D$ network presented in the main text.

IV. MODE ANALYSIS OF THE 2D ATN NEAR EQUILIBRIUM.

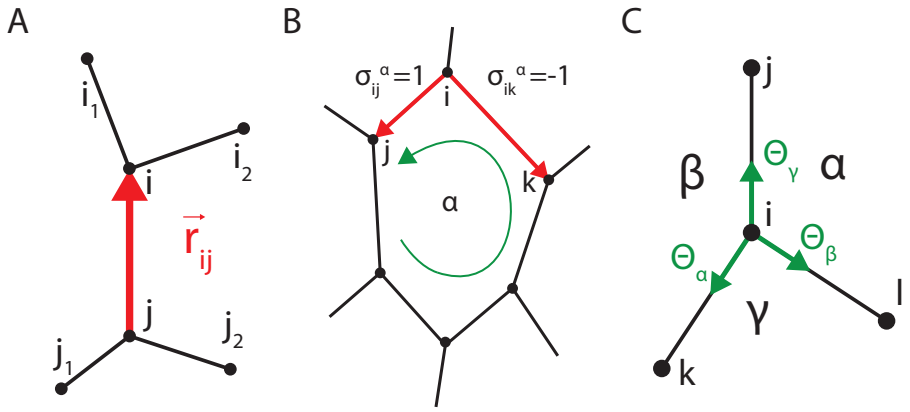

FIG. 2. (A) Labeling of edge vector $\boldsymbol{r}_{ij}$ along with vertices connected along all 4 neighboring edges used in Eq. (SI24). (B) Definition of circular sum around a cellular plaquette for Eq. (SI25). We define the positive direction to be counter clockwise around each cell. If the edge points 'up-stream' $\sigma^{\alpha}_{ij} = -1$ as shown. (C) Vertex i can also be labeled by the triplet of cells that meet at vertex i, in this case $\alpha\beta\gamma$. Isogonal deformations act along the 'external' edge to the cell.

The two-dimensional dynamics near equilibrium is most naturally expressed in terms of edge vectors $\boldsymbol{r}_{ij}$. Equations of motion can be derived directly from Eq. $2-4$ in the main text. Hereafter time is rescaled $t \to \frac{K}{\nu}t$ to reduce the appearance of unnecessary constants.

$$\frac{d}{dt}\boldsymbol{r}_{ij} = \boldsymbol{u}_{i_1 i} + \boldsymbol{u}_{i_2 i} + \boldsymbol{u}_{j j_1} + \boldsymbol{u}_{j j_2} - 2\boldsymbol{u}_{ij} \tag{24}$$

where $\boldsymbol{u}_{ij} \equiv K^{-1} T_{ij} \hat{\boldsymbol{r}}_{ij} = u_{ij} \hat{\boldsymbol{r}}_{ij}$ and neighboring vertices are defined in Fig. 2a. Parameterization in terms of edge vectors simplifies the resultant algebra at the cost of introducing $2c$ additional degrees of freedom associated to the geometric constraint that edge vectors sum to zero around each cellular plaquette

$$\sum_{<i,j> \in \mathcal{E}_\alpha} \sigma_{ij}^\alpha \, \boldsymbol{r}_{ij} = 0 \quad \forall \alpha \tag{25}$$

$\mathcal{E}_\alpha$ denotes the set of all edges associated to cell α while $\sigma_{ij}^\alpha = \pm 1$ if $\boldsymbol{r}_{ij}$ points counter-clockwise or clockwise respectively, as graphically shown in Fig. 2b. It is easy to check that dynamics described by Eq. (SI24) preserves the constraint defined by Eq. (SI25) - each vertex's equation of motion will appear in the sum twice with opposing signs. We linearize Eq. (SI24) and decompose each edge vector into transverse $\delta\theta_{ij}$ and longitudinal δr_{ij} components defined by

$$\delta \boldsymbol{r}_{ij} = \delta r_{ij} \, \hat{\boldsymbol{r}}_{ij} + r_{ij} \, \delta\theta_{ij} \, (\hat{\boldsymbol{z}} \wedge \hat{\boldsymbol{r}}_{ij}) \tag{26}$$

leaving us with equations

$$\frac{d}{dt} \delta r_{ij} = \sum_{<k,l>} \left[L_{ij;kl} \, \delta u_{kl} - A_{ij;kl} \, u_{kl} \delta\theta_{kl} \right] \tag{27}$$

$$r_{ij} \frac{d}{dt} \delta\theta_{ij} = \sum_{<k,l>} \left[A_{ij;kl} \, \delta u_{kl} + L_{ij;kl} \, u_{kl} \delta\theta_{kl} \right] \tag{28}$$

where we have defined

$$L_{ij;kl} \equiv \hat{\boldsymbol{r}}_{ij} \cdot \hat{\boldsymbol{r}}_{kl} \left[\mathcal{A}_{ki} \delta_{li} + \mathcal{A}_{lj} \delta_{kj} - \mathcal{A}_{li} \delta_{ki} - \mathcal{A}_{kj} \delta_{lj} \right]$$
$$A_{ij;kl} \equiv \hat{\boldsymbol{r}}_{ij} \wedge \hat{\boldsymbol{r}}_{kl} \left[\mathcal{A}_{ki} \delta_{li} + \mathcal{A}_{lj} \delta_{kj} - \mathcal{A}_{li} \delta_{ki} - \mathcal{A}_{kj} \delta_{lj} \right]$$

$\mathcal{A}_{ij}$ is the adjacency matrix of the cell array, i.e. is one only if vertex i and j are connected, and δ_{ij} is the Kronecker delta. Dynamics of small perturbations in intrinsic length is found by expanding Eq. (3) from the main text about the fixed point

$$\frac{d}{dt} \delta \ell_{ij} = \kappa_{ij} \left[\delta u_{ij} - \delta m_{ij} \right] \tag{29}$$

where

$$\kappa_{ij} \equiv \frac{\nu \ell_{ij} W'(1)}{\tau_\ell K u_{ij}} \tag{30}$$

Tension dynamics is easily obtained via the constitutive relation $u_{ij} = r_{ij} - \ell_{ij} = T_{ij}/K$

$$\frac{d}{dt} \delta u_{ij} = \frac{d}{dt} \delta r_{ij} - \kappa_{ij} \delta u_{ij} + \kappa_{ij} \delta m_{ij} \tag{31}$$

Lastly, the myosin dynamics is governed by

$$\frac{d}{dt} \delta m_{ij} = \bar{\alpha} \left(\delta u_{ij} - \delta m_{ij} \right) \tag{32}$$

where myosin has been rescaled to have units of interfacial deformation: $\delta m_{ij} \to a T_s K^{-1} \delta m_{ij}$ and $\bar{\alpha} \equiv \alpha \nu K^{-1} \tau_\ell^{-1} W'(1)$. Isogonal modes correspond to $\delta\theta = \delta u = 0$ which is realized by $\delta \ell_{ij} = \delta r_{ij}$, provided $\sum_{<i,j> \in \mathcal{E}_\alpha} \sigma_{ij}^\alpha \, \delta r_{ij} \hat{\boldsymbol{r}}_{ij} = 0$. The latter constraint is satisfied for

$$\delta \boldsymbol{r}_i = \hat{\boldsymbol{r}}_{ji} \frac{T_{ji} \Theta_\gamma}{S_i} + \hat{\boldsymbol{r}}_{ki} \frac{T_{ki} \Theta_\alpha}{S_i} + \hat{\boldsymbol{r}}_{li} \frac{T_{li} \Theta_\beta}{S_i} \tag{33}$$

where $\delta \boldsymbol{r}_i$ denotes displacement of vertex at which adjacent cells α, β, γ meet; $\Theta_\alpha, \Theta_\beta, \Theta_\gamma$ are independent variables associated with isogonal modes of the denoted cells and S_i denotes the area of said vertex's dual triangular plaquette. A graphical depiction of this concept is shown in Fig. 2c. We check Eq. (SI33) leaves edge angles unchanged.

$$\boldsymbol{T}_{ij} \wedge [\delta \boldsymbol{r}_i - \delta \boldsymbol{r}_j] = 2 \left[\frac{\boldsymbol{T}_{ij} \wedge \boldsymbol{T}_{i_1 i}}{S_i} \Theta_\alpha + \frac{\boldsymbol{T}_{ij} \wedge \boldsymbol{T}_{i_2 i}}{S_i} \Theta_\beta - \frac{\boldsymbol{T}_{ij} \wedge \boldsymbol{T}_{j_1 j}}{S_j} \Theta_\alpha - \frac{\boldsymbol{T}_{ij} \wedge \boldsymbol{T}_{j_2 j}}{S_j} \Theta_\beta \right] = 0$$

Thus, isogonal deformations have no restoring force. Eqs. (SI27-SI28) and (SI31-SI32) fully specify the closed form linearized dynamics with matrix H that can be expressed

$$S = U^{-1} H U \tag{34}$$

where $U \equiv \text{diag}\left[1, 1, \sqrt{u_{ij} r_{ij}}, \sqrt{\frac{\kappa_{ij}}{\bar{\alpha}}}\right]$ and

$$S \equiv \begin{pmatrix} 0 & L_{ij;kl} & -A_{ij;kl} & 0 \\ 0 & L_{ij;kl} - \kappa_{ij}\delta_{ij;kl} & -A_{ij;kl}\sqrt{\frac{u_{kl}}{r_{kl}}} & \sqrt{\bar{\alpha}\kappa_{ij}}\delta_{ij;kl} \\ 0 & \sqrt{\frac{u_{ij}}{r_{ij}}} A_{ij;kl} & \sqrt{\frac{u_{ij}}{r_{ij}}} L_{ij;kl} \sqrt{\frac{u_{kl}}{r_{kl}}} & 0 \\ 0 & \sqrt{\bar{\alpha}\kappa_{ij}}\delta_{ij;kl} & 0 & -\bar{\alpha}\delta_{ij;kl} \end{pmatrix}$$

Because the first column of the matrix is equal to zero, δr_{ij} is slaved to other components and thus the rank of H is at most $9c$ as our null space contains c isogonal modes defined above, along with the $2c$ geometric constraints (see Eq. (SI25)) that are conserved by the dynamics. The left eigenvectors of isogonal modes were numerically found to be exponentially localized around the respective cell with a length scale $(\kappa + \bar{\alpha})^{-1/2}$: i.e. they are only forced with the screening length set by contractility as shown in Fig. 4(a). This reproduces the result found in $1D$.

The reduced matrix $\tilde{S}$ is obtained by eliminating the 1^{st} row and 1^{st} column of S. It is manifestly symmetric in our chosen basis, following immediately from the fact that $L_{ij;kl}$ and $A_{ij;kl}$ are symmetric and anti-symmetric respectively. Furthermore, it is easy to see that $L_{ij;kl}$ satisfies all properties of a normalized weighted graph Laplacian defined over edges in our triangulation and thus will be negative semi-definite, as shown in Fig. 3, ensuring stability of the tension-triangulation of the unperturbed ATN state. $\bar{\alpha} > 0$ introduced acoustic branches and thus phonons at long times. Thus we conclude that $2D$ modes will exhibit (albeit in a more complex form) qualitatively equivalent features as that derived for the $1D$ cable above - solid-like phonons with weak spring constants at long time and short-scale liquid like behavior dominated by isogonal deformations.

Another important characterization of the normal modes is the structure of eigenmodes: are they localized or extended? To address this question we numerically measured the distribution of participation ratios, defined as

$$p_{n'} \equiv \sum_{n=1}^{N} |\phi_n^{n'}|^4 \tag{35}$$

where $\phi_n^{n'}$ represents the n^{th} component of the flattened eigenvector $\begin{pmatrix} \delta r_{ij} & \delta u_{ij} & r_{ij}\,\delta\theta_{ij} & \delta m_{ij} \end{pmatrix}^T$ and $n, n' \in [1, N]$ where N denotes the system size. If $\phi^{n'}$ is extended, then $|\phi_n^{n'}| \sim 1/\sqrt{N}$ and thus $p_{n'}$ should scale with inverse system size. Similarly, if $\phi^{n'}$ is localized, it should saturate to a finite number with increasing N. We tested the localization of our modes by tracking how the distribution of $p_{n'}$ scaled with increasing number of cells within hexagonal and randomly generated voronoi lattices. Isogonal modes were excluded from analysis as it is known a priori that each is localized to a single cell. All non-isogonal modes are fully extended in the hexagonal case - the system is diagonalizable in a plane-wave basis - as shown numerically in Fig. 4b. Conversely, as shown in Fig. 4c, it was found that all but one band of 'transverse' modes localize for disordered Voronoi lattices. In other words, c modes are still fully extended on a disordered triangulation.

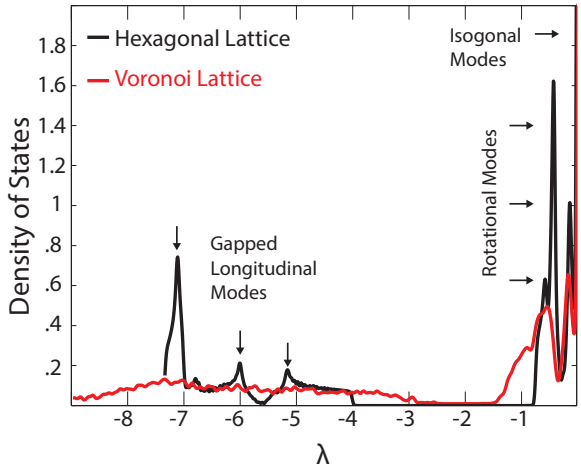

FIG. 3. "Density of states" plot for the normal modes of H governing the dynamics of fluctuations about the ATN equilibrium corresponding to i) a hexagonal array (black line) and ii) a randomly generated Voronoi tesselation (red line). In both cases $3c$ modes lie at zero, of which c are the isogonal modes and the remaining $2c$ correspond to geometric constrains (on edge vectors). The rest of the eigenvalues are negative as required by stability. 1/3 of the modes (in the hexagonal lattice case) are separated from zero by a gap proportional to the activity parameter q.

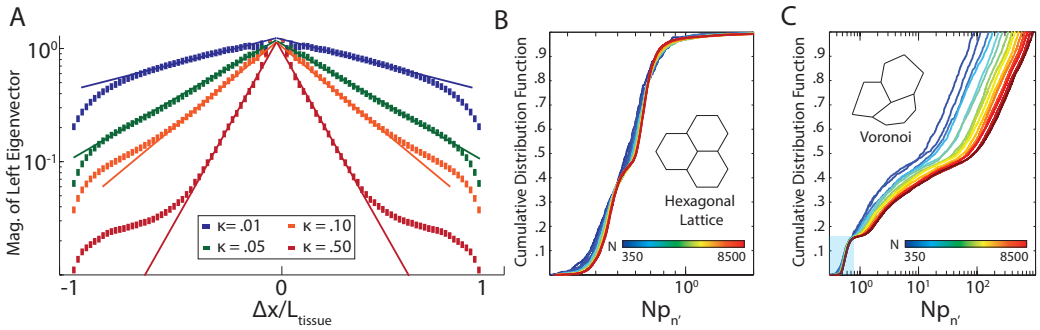

FIG. 4. (a) Eigenvectors associated to isogonal modes fall off exponentially with the characteristic length scale of decay $\sim \kappa^{-1/2}$. Points correspond to left eigenvectors obtained by numerical diagonalization of H; solid lines are decaying exponentials with characteristic length $\kappa^{-1/2}$. (b) Eigenmode structure for regular hexagonal and Voronoi lattices: fraction of eigenmodes (excluding isogonal modes) below a given participation ratio $Np_{n'}$ (defined by Eq. SI35)) scaled with the number of cells N. All modes are extended as indicated by the collapse of curves scale on top of each other. (c) Repeated for random Voronoi lattices of varying size. In contrast to the case (b), only 1/7 of the modes (highlighted in light blue) are extended, while 6/7 are localized, as indicated by the lack of curve collapse.

V. CONSTRUCTION OF THE CONTROL DISTRIBUTION OF χ AND ITS TESTS ON SYNTHETIC DATA

The appeal of the geometric compatibility constraint (c.f. Eqn 5 in main text) is that one can directly measure it from images of an epithelial tissue and thus immediately test the validity of force balance and tension dominance assumptions. Alas, even if the assumptions were correct, one would not expect this constraint to be satisfied exactly by empirical data because of i) the measurement noise (imperfect image segmentation as well as fundamental digitization of vertex positions) and the ii) dynamical fluctuations of cells. Hence our analysis focuses on the probability density function (PDF), $P(\log\chi)$, and evaluates the tendency towards $\log\chi = 0$ (i.e. constraint satisfaction) which manifests itself as a statistically significant

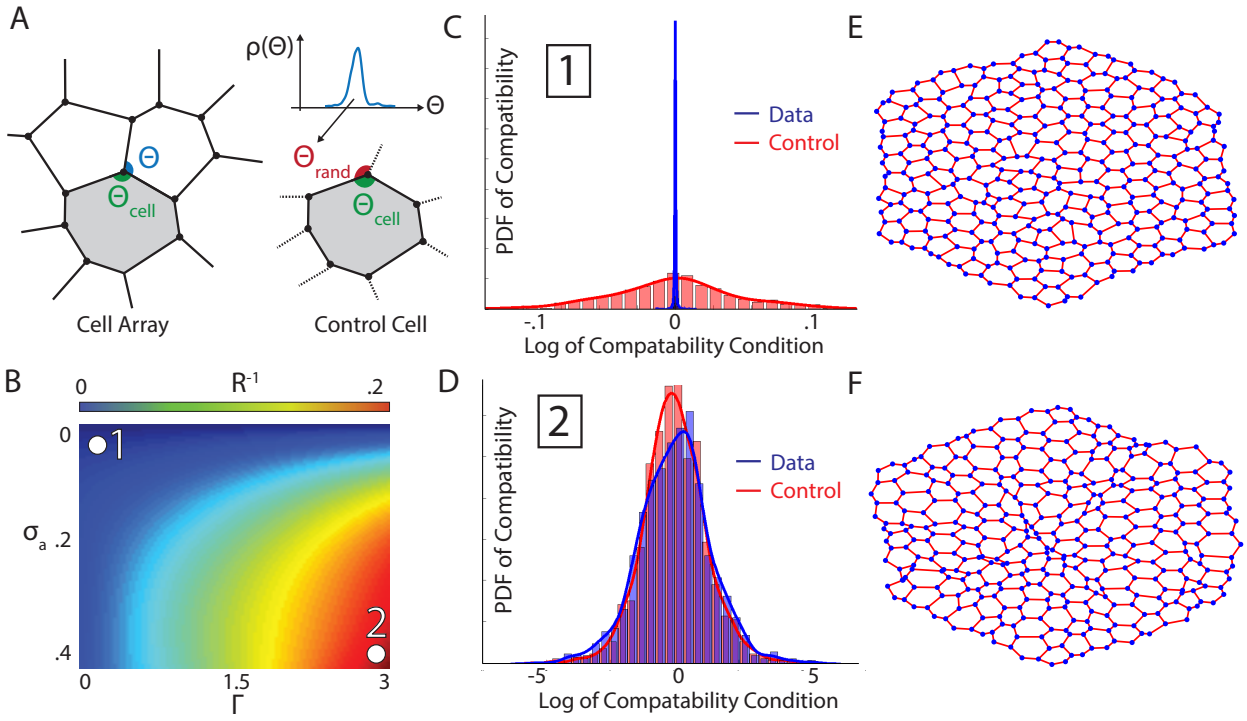

FIG. 5. (a) A diagram depicting the construction of the control distribution. Cells are sampled from the array and given randomized external edges consistent with the empirical angle distribution of the tissue. (b) A heatmap, in the space of vertex model parameters σ_a and Γ, defined by Eq. SI36, of average edge curvature in units of the edge length, $R^{-1}r$. In a static tension-net, cell edges are straight lines hence curvature is exactly zero. This is found in the upper-left corner. Conversely, as the area parameters become large, the lattice approaches a regime where pressure can no longer be neglected, found in the lower right corner. (c-d) Two histograms of the compatibility condition measured from synthetic cell arrays. Numbers match the numbered points in (b). As $\Gamma, \sigma_a \to 0$ we approach our static tension net limit. As expected, for parameters corresponding to point 1, the vertex-model generated synthetic tissue exhibits a compatibility measure, $\log \chi$, tightly clustered around zero relative to the null distribution. Parameters for point 2 are in the regime where pressure differentials between cells are important and as can be seen, the tension network approximation is not valid. In this case, the distribution of $\log \chi$ is statistically consistent with the control. (e-f) Representative geometry of the cell arrays corresponding to vertex model parameters used to generate the histograms given in (c-d) respectively.

reduction of variance compared to a randomized "control distribution" that corresponds to mechanically unconstrained cell arrays (or convex polygonal tessellations of a plane) consistent with the observed angles of the real tissue. Below we discuss the exact construction of the control distribution and elucidate its discriminatory power using synthetic data. Furthermore, we expand upon potential tests one can use to analyze potential sources of the measured variation.

It is important to note that the average $\langle \log(\chi) \rangle = \frac{1}{c} \sum_\alpha \log(\chi_\alpha)$ is determined entirely by χ_α from the cells on the *boundary* of the tissue. When computing the mean, each lattice angle in the bulk will be summed over twice with opposing signs and thus the only contribution comes from angles along the boundary. This is just a discrete manifestation of Stokes' law. Since the number of boundary cells scales as $\sqrt{c}$ for $c \gg 1$, the average goes to zero as $1/\sqrt{c}$. Hence, empirically $P(\log \chi)$ is approximately normal with zero average.

The control distribution is constructed as follows. A random cell is sampled from the segmented cell array. Each vertex of the sampled cell is *given* a random external edge using a vertex angle sampled from the empirical angle distribution. The remaining angle is simply the supplementary of the interior angle of the cell plus the randomly sampled angle. To ensure convexity, the configuration is accepted provided no angle greater than π was generated. A graphical depiction of this procedure is given in Fig. 5a. This procedure

is repeated a sufficient number of times to ensure the distribution is well sampled (set to $10x$ the number of cells in the array). Hence, the control distribution measures the 'maximum' variance possible in $\log(\chi)$ given just the set of observed lattice angles. We then compare the variances between the measured PDF and the control: $\sigma_{data}/\sigma_{null} << 1$ signifies statistically significant tendency of the observed array geometry towards small values of χ and hence approximate compatibility.

To validate the proposed statistical test, we examined synthetic data constructed by minimizing a vertex-type model energy function which allows for variation of internal pressure of cells $p_\alpha = 2\Gamma(A_\alpha - \bar{A}_\alpha)$ while making edges Hookean springs with randomized intrinsic lengths ℓ_{ij}:

$$E = \sum_{<i,j>} (r_{ij} - \ell_{ij})^2 + \Gamma \sum_{\alpha} (A_\alpha - \bar{A}_\alpha)^2 \tag{36}$$

Intrinsic cell area $\bar{A}_\alpha$ is to be a quenched random number sampled from a Gaussian distribution with mean $3\sqrt{3}/2$ and standard deviation σ_a. Furthermore, intrinsic edge length ℓ_{ij} is sampled from a Gaussian distribution with mean 1 and standard deviation fixed to be .2. The external space has pressure -1 to balance the internal tension of the vertex model. Cell arrays are obtained by minimization of E (approximately 300 cells were relaxed per iteration) under the prescribed boundary conditions. We then construct $P(\log\chi)$ distributions for the generated cell arrays for different values of Γ and σ_a and compare to corresponding control distributions. This allows us to estimate the ratio $\sigma_{data}/\sigma_{null}$ as a function of pressure's contribution to mechanical equilibrium.

To quantify the effect of pressure fluctuations (forced in the model by heterogeneity of $\bar{A}_\alpha$), we compute the curvature (normalized to average edge length) $R^{-1} \equiv \frac{\Delta p r}{T}$ of each edge as defined by the Young-Laplace Law, which relates the radius of curvature of the interface R^{-1} to edge tension T and the pressure difference Δp across the edge. Average curvature $\langle R^{-1}\rangle$ is a convenient measure of the extent of pressure contribution to the force balance relative to tension. Fig. 5b displays a heat map showing $\langle R^{-1}\rangle$ obtained for different values of Γ and σ_a. Representative examples exhibiting the discrimination of our control distribution between the case of a tension network (marked by the point labeled 1) and a network with non-negligible pressure contribution (point 2) are shown in Fig 5(c-d). Examples of cell array geometries for each range of vertex model parameters are shown in Fig. 5(e-f). As expected, while the 1st case (Fig. 5c) passes our statistical test for compatibility, the 2nd case (Fig. 5d) fails.

The above vertex model allowed us to quantitatively study the effect of pressure differentials, captured by $\langle R^{-1}\rangle$, and measurement error associated to the discretization of vertex positions on an image on the variance of $P(\log\chi)$. 'Pixelation' noise, denoted σ_{pix}, was introduced by scaling tissues obtained from minimization of Eq. (SI36) to match the desired edge length and then rounding vertex position to the nearest integer. Both the resultant standard deviation of the $\log(\chi)$ distribution as well as the ratio $\sigma_{data}/\sigma_{null}$ are reported in Fig. 6e,f. As expected, σ_χ increases as pressure differences become non-negligible ($\langle R^{-1}\rangle > .1$) and as measurement uncertainty increases. These results provide a baseline to which to compare data.

Furthermore, as cell edge curvature can be directly measured from high quality images of epithelial tissues, we can estimate both $\langle R^{-1}\rangle$ and σ_{pix} parameters corresponding to real tissues. In Fig. 6e,f we place on the heat maps the points corresponding to the pupal notum, ventral mesoderm, lateral ectoderm, and larval wing disc epithelia (marked respectively as the triangle, square, circle and star) for comparison with results below. Curvatures were estimated by fitting segmented edges to circles.

All four analyzed tissues are shown in Fig 6: ventral mesoderm prior to invagination, pupal notum, lateral ectoderm during early germ band extension, and third instar larval imaginal wing disc (data kindly provided by Ken Irvine [4]). Example images of the analyzed data are shown in Fig. 6a-d. The measured ratios $\sigma_{data}/\sigma_{control}$ were found to be consistent with synthetic ratios of their estimated positions on Fig. 6f and thus we conclude both the ventral mesoderm and pupal notum are well approximated as quasistatic tissues in tension-balance.

Lastly, we tested the prediction that the observed increase in σ_{data} between the lateral ectoderm and the ventral mesoderm and pupal notum is primarily due to neglected curvature. Specifically, using Eq. (SI8) one can quantitatively analyze the fraction of the measured variance of $\log\chi$ that originates solely from the contribution of pressure differentials to mechanical equilibrium. To this end, we analyzed the lateral ectoderm tissue and estimated the compatibility measure predicted from the small, yet non-negligible pressure differentials between neighboring cells. We found good agreement between $\log(\chi_{est})$, the quantity

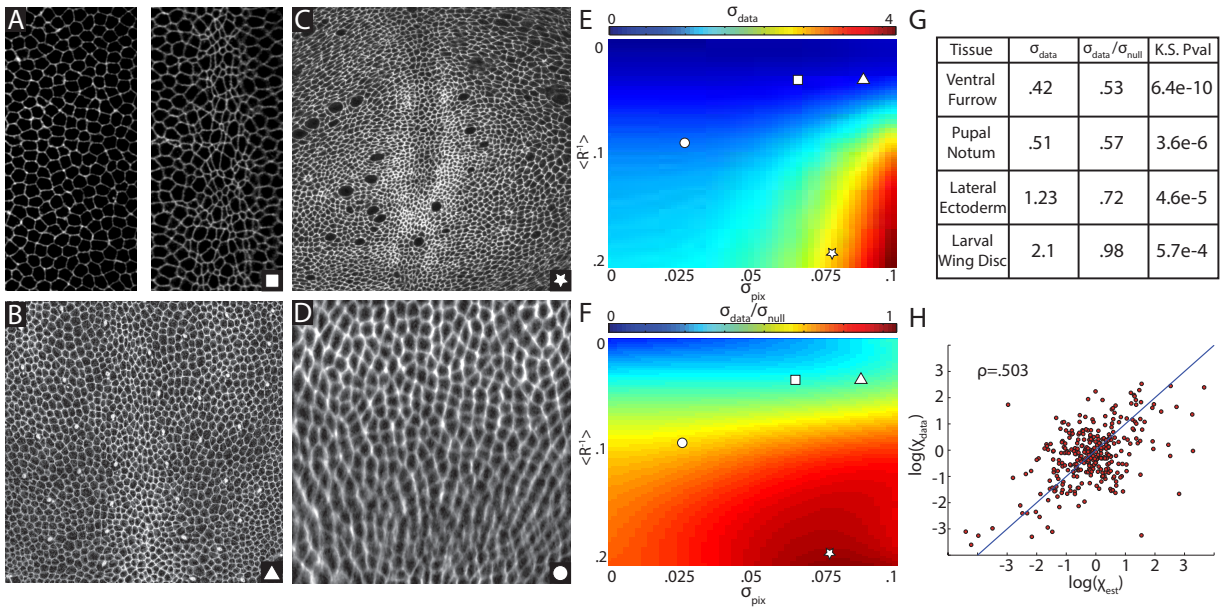

FIG. 6. (a) An image of the ventral mesoderm (*Drosophila* embryo) before invagination of the ventral furrow; (b) Pupal notum epithelium; (c) Epithelium of the wing imaginal disc at the third instar larval stage; (d) Embryonic lateral ectoderm during early germ band extension; (e) A heatmap of the standard deviation of $\log(\chi)$ (obtained via synthetic data created minimizing the energy of Eq. (SI36)) as a function of both average edge curvature R^{-1}, normalized to average edge length, and measurement noise σ_{pix}, simulated by introducing rounding error in vertex position. The triangle, square, circle, and star markers denote the estimated positions of the pupal notum, ventral furrow, lateral ectoderm, and wing disc epithelia respectively. (f) The analogous plot to (e) showing the ratio $\sigma_{data}/\sigma_{null}$. As curvature and measurement noise increase, the ratio tends toward 1 as expected. Again the estimated positions of each tissue is marked. (g) Characterization of the distribution of the compatibility measures for the four tissues. (h) A scatter plot comparing the measured log compatibility condition against the predicted value using Eq. (SI8) and empirically measured cell edge curvatures in the lateral ectoderm. The correlation coefficient is approximately .5 giving us confidence that half of the variance of the empirical compatibility condition comes from a violation of our constant pressure assumption. The number of cells used in this analysis was 328.

predicted from Eq. (SI8), and the empirically measured value $\log(\chi)$ (Pearson's correlation coefficient of $\sim .5$ for 328 cells) as shown in Fig. 6h . As such, we conclude that roughly half of the observed variance of $P(\log\chi)$ can be explained solely by observed curvatures, again consistent with estimates obtained from the synthetic data.

VI. PROCEDURE USED TO FIT ISOGONAL DEFORMATION DURING VENTRAL FURROW FORMATION

To define isogonal transformations from observed vertex displacements we use as a starting point Eqn. (6) of the main text, reproduced here

$$\delta \boldsymbol{r}_{\alpha\beta\gamma} = \hat{\boldsymbol{r}}_{\alpha\beta}\frac{T_{\alpha\beta}\Theta_\gamma}{S_{\alpha\beta\gamma}} + \hat{\boldsymbol{r}}_{\beta\gamma}\frac{T_{\beta\gamma}\Theta_\alpha}{S_{\alpha\beta\gamma}} + \hat{\boldsymbol{r}}_{\gamma\alpha}\frac{T_{\gamma\alpha}\Theta_\beta}{S_{\alpha\beta\gamma}} \tag{37}$$

This immediately introduces two problems: (i) we must track vertices over time to measure the deformation field $\delta\boldsymbol{r}_{\alpha\beta\gamma}$ and (ii) since $T_{\alpha\beta}$ and $S_{\alpha\beta\gamma}$ are defined by the dual tension triangulation, we must infer, from the observed cell array at a given time, the closest exactly-compatible cell array and its corresponding dual triangulation. The latter amounts to 'inferring' the tensions from the observed cell array, i.e. carrying out

a "Mechanical Inverse" [1] under the assumptions of the ATN model. This was done by exploiting the fact that edges of the constructed tension triangulation are *orthogonal* to the 'dual' edge of the cell array - i.e. $[\boldsymbol{Q}_\alpha - \boldsymbol{Q}_\beta]\cdot\hat{\boldsymbol{r}}_{ij} = 0$ where cells α, β border the edge that runs between vertices i, j and $\boldsymbol{Q}_\alpha$ denotes the vertex of the tension triangulation that corresponds to cell α. Hence the 'closest' possible tension triangulation is inferred by minimizing the following energy function with respect to the dual triangulation vertices $\{\boldsymbol{Q}_\alpha\}$.

$$E\left[\{\boldsymbol{Q}_\alpha\}|\hat{\boldsymbol{r}}_{ij}\right] = \sum_{<\alpha,\beta>}\left[\left[\boldsymbol{Q}_\alpha - \boldsymbol{Q}_\beta\right]\cdot\hat{\boldsymbol{r}}_{ij}\right]^2 + \Lambda\left[\frac{1}{E}\sum_{<\alpha,\beta>}\left[\boldsymbol{Q}_\alpha - \boldsymbol{Q}_\beta\right]^2 - 1\right] \tag{38}$$

Λ is a Lagrange multiplier used to fix the scale of tensions and exclude the trivial solution (all triangulation vertices lying on top of each other). MATLAB's function *fmincon* was used to minimize using the 'active-set' algorithm (where the centroid of the graph is constrained to the origin). The resultant $\{\boldsymbol{Q}_\alpha\}$ provide the geometric factors of the triangulation that directly enter the matrix entries defined by Eqn. (SI37). Predicted tensions as well as the cumulative distribution is shown in Fig. 7 (ab) respectively for a snapshot of the Ventral Furrow formation.

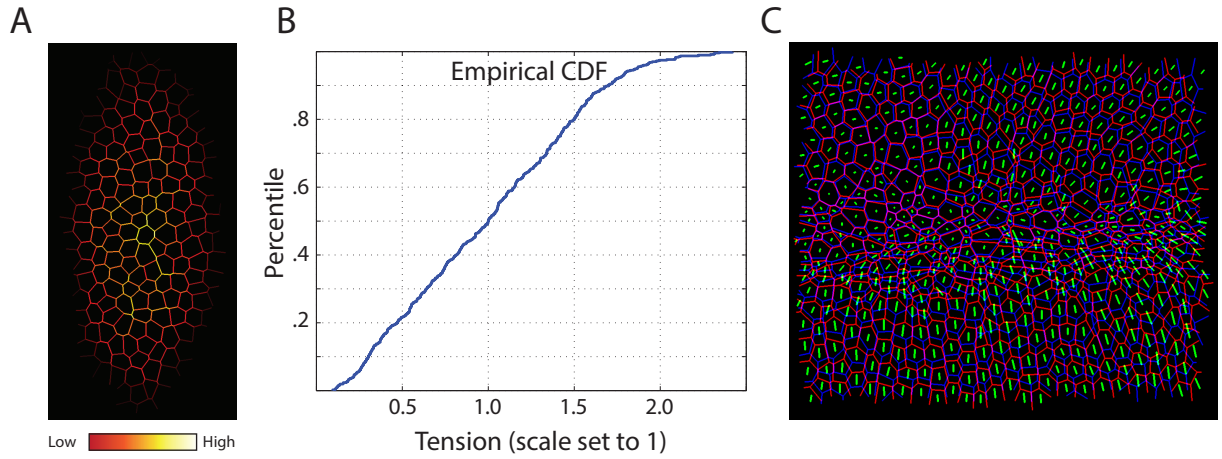

FIG. 7. (a) A heatmap illustrating the distribution of tensions on the ventral side of the embryo minutes before ventral furrow formation. The 'hotter' the color, the higher the tension. (b) A cumulative distribution function of all estimated balanced tensions within the cell array shown in (a). Due to the assumption of force balance the scale is unknown and thus the mean tension is set to 1. The distribution is relatively uniform. (c) Example of cell tracking algorithm pairing segmented cells in subsequent time-points.

Vertices were tracked by tracking cells via dominant pixel overlaps and using the tracked cells to define vertex displacements $\delta\boldsymbol{r}_{\alpha\beta\gamma}$ for successive time points by looking for vertices that share the same three bordering cells. Deformation fields were computed over 20 second time windows. While T1 events were rare during ventral furrow formation, a handful were observed in each of the 5 movies analyzed. In the event of a T1 transition, unpaired vertices are 'tracked' using a point-matching algorithm - i.e. the vertex will get paired with the closest unpaired vertex in the subsequent time-point. If there is no close candidate to the vertex, a displacement vector is interpolated onto the unpaired vertex. These displacements were directly used on the L.H.S. of Eqn. (SI37). An example of tracked cells (plotted with tracers) is shown in Fig. 7c.

Eqn. (SI37) is a rectangular ($2v$ by c) linear system of equations defining vertex displacements corresponding to an arbitrary isogonal transformation parameterized by $\{\Theta_\alpha\}$ and can be solved by simple least squares analyses. This problem is heavily over-constrained ($2v = 4c$ as compared to c fitting parameters) and thus represents a strong test of our model.

VII. DISCUSSION OF VENTRAL FURROW ATN MODEL FOR *TWIST* AND *SNAIL* MUTANTS

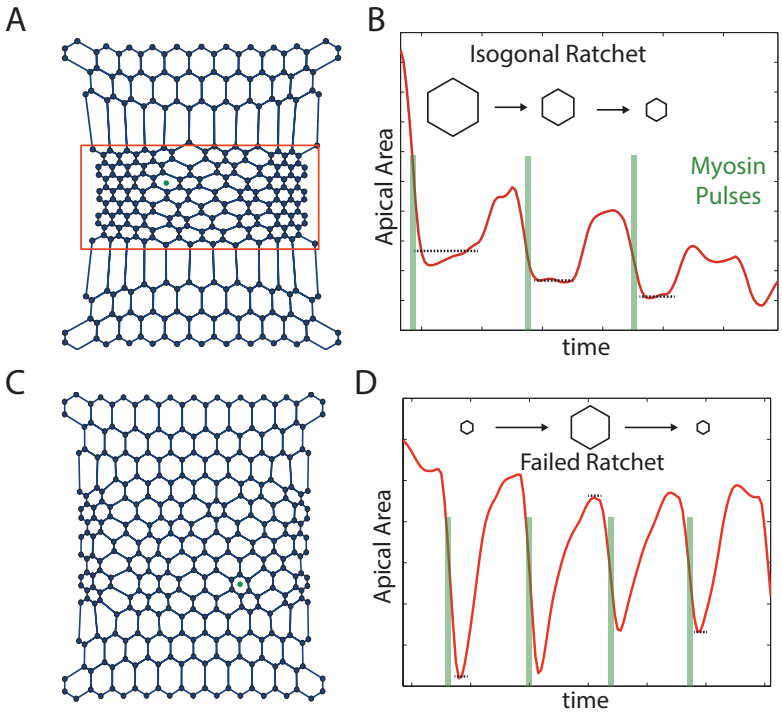

FIG. 8. (a) Plot of the simulated active tension net with bulk medial myosin pulses within the red box. (b) A characteristic time-course of apical area of single cell during the simulation - denoted in (a) with a green dot. Cell contracts as a result of medial myosin pulses and subsequently stabilizes at a smaller area (until its neighbor is pulled). Three such pulses are shown. (c) The analogous plot to (a) but in the model with reduced tension $T \sim \Delta p\, r$. As pressure can no longer be neglected, cells by and large recover their apical area and do not show net constriction. (d) The time-course of apical area of cell marked with green dot in (c). The constriction fails to stabilize at a smaller area due to the influence of pressure. The result is large area fluctuations (due to small cortical tension) that do not permanently constrict.

The main text presented the ATN model interpretation of the dynamics of apical constriction preceding invagination of the ventral mesoderm of *WT* embryos as well as discussed *twist* and *snail* phenotypes in the context of the ATN model. In particular, we interpret the "ratchet" mechanism described by [5] in terms of a systematic drift of the cell array geometry along the manifold of tension -balanced states, driven by the pulsatile medial acto-myosin activity. The observed VF formation defect in *snail* mutants is associated with its failure to generate medial myosin pulses. Conversely, the interpretation of *twist* mutant is more subtle: Martin *et al* [5] attributed it to the failure of cells to remodel their cortical cytoskeleton to "trap" the transient apical constriction, which leads to the failure of the ratcheting process. In the main text we proposed that the *twist* phenotype may be understood in the framework of the ATN model simply as a consequence of lower tension in the cortical cytoskeleton resulting in non-negligible pressure heterogeneity that lifts the degeneracy of the tension-balance manifold and thus introduces a restoring force for isogonal deformations. Below we illustrate this scenario by a computer simulation of a vertex-type model using ATN dynamics.

Simulation of the WT phenotype was initialized to a rectangular array of hexagonal cells with unit edge length. Equations (2-3) were simulated on each edge under the assumption of a constant, uniform myosin field. Each cell's pressure was taken to be $2\Gamma\left[A_\alpha - \bar{A}_\alpha\right]$ with $\bar{A}_\alpha = 3\sqrt{3}/2$ (the area of a hexagon with a

unit edge) for all cells in the mesoderm. Effects of the medial myosin pulse were simulated via a transient isotropic perturbation of tensions around cells (with amplitude comparable to the scale of cortical tension). Inter-arrival times between myosin pulses were Gaussian distributed and randomly sampled for each cell in the marked furrow (see red box in Fig. 8a). No pulses were simulated outside of the synthetic furrow. To represent *twist* phenotype we carried out a similar simulation, but with the tension scale reduced by a factor of 10 so that $T \sim \Delta pr$. This moved the system out of the tension-net regime, causing the area-elasticity term to 'force' retraction of the cell after contractions caused by the myosin pulse. Randomizing $\bar{A}_\alpha$ magnified the stabilization defects - intended to simulate potential effects of the lack of a persistent medial actin network. Plots of the final lattice as well as representative time-traces from synthetic cells are shown in Fig 8cd.

VIII. IMAGE ANALYSIS METHODS

All images were first classified using machine learning software Ilastik [7]. The resultant probability map was passed into MATLAB and segmented using the watershed algorithm [8] after pre-filtering. Once segmented, all relevant quantities such as vertex positions and lists of neighboring cells and edges were stored in a custom data structure. All code is available upon request.

Myosin was measured using edges obtained from the segmentation produced via the watershed algorithm and dilated by one pixel to account for potential segmentation error. The average intensity over the set of pixels was used as a proxy for myosin line density for each edge. As we only cared about myosin dynamics up to an overall scale, the relative myosin was computed and then tracked over time - i.e. we divided by the instantaneous mean. Edges were tracked using the tracked cell data.

Tracking (matching segmentation labels between subsequent time-points) was done using point-matching of cell centroids after correcting for PIV (Particle Image Velocimetry) estimated flow fields between time points. PIV flow fields were estimated using cross-correlation between gridded regions defined on our image [9] With cell's tracked, vertices and edges can be easily tracked using their bordering cells.

IX. SIMULATION METHODS

Eqs. (2-4) in the main text were numerically integrated using MATLAB's ODE15s solver as the large time-scale separation resulted in a stiff system. T1 events were handled using MATLAB's event feature, if an edge falls below a critical user-specified value, then we flag an event which stops the integration. A T1 event is manually performed and then numerical integration is restarted.

For the 2D rheology simulation, a 15 x 15 square of cells was initialized in a slightly disordered hexagonal lattice under constant pressure to balance against the internal tension. Sinusoidal external forces were attached to the vertices on the vertical boundary. Strain rate was measured on vertical junctions throughout the bulk.

[1] Chiou, K. Hufnagel, L. Shraiman, B. (2012). Mechanical stress inference for two dimensional cell arrays. *PLOS Comp. Bio.*, 8(5)

[2] Pinkall, U., Poltheir, K. (1993). Computing discrete minimal surfaces and their conjugates. *Exp. Math.*, 2(1):15-36

[3] Villain, J. (1980) Two-Dimensional Solids and Their Interaction with Substrates. *Ordering in strongly fluctuating condensed matter systems*, ed. T. Riste (Plenum, New York), p. 221

[4] Rauskolb, C, et al. (2014). Cytoskeletal Tension Inhibits Hippo Signaling through an Ajuba-Warts Complex. *Cell*, 158:143-156

[5] Martin, AC. Kaschube, M. Wieschaus, E. (2009). Pulsed contractions of an actin-myosin network drive apical constriction. *Nature*, 457(7228):495-9

[6] Mason, F. Tworoger, M., Martin, A. (2013). Apical domain polarization localizes actinmyosin activity to drive ratchet-like apical constriction. *Nature*, (15): 926936

[7] Sommer, C., Strhle C., Kthe U., Hamprecht, F. A. (2011). ilastik: Interactive Learning and Segmentation Toolkit. *Eighth IEEE International Symposium on Biomedical Imaging (ISBI). Proceedings* 230-233.

[8] Meyer, F. (1994). Topographic distance and watershed lines. *Signal Processing* 38:113-125
[9] Keane, R.D., Adrian, R.J. (1992) Theory of cross-correlation analysis of PIV images. Applied Scientific Research 49: 191.